Title

Thermoeconomic cost optimization of superconducting magnets for proton therapy gantries

Journal

Superconductor Science and Technology, 33(10)

ISSN

0953-2048

Authors

Teyber, Reed

Brouwer, Lucas

Godeke, Arno

et al.

Publication Date

2020-10-01

DOI

10.1088/1361-6668/abaa53

Peer reviewed

Thermoeconomic Cost Optimization of Superconducting Magnets for Proton Therapy Gantries

Reed Teyber[1], Lucas Brouwer[1], Arno Godeke[2], Soren Prestemon[1]

[1]Lawrence Berkeley National Laboratory, Berkeley, CA 94720

[2]Varian Medical Systems Particle Therapy GmbH, Troisdorf, Germany 53842

E-mail: rteyber@lbl.gov

Abstract.

A compact gantry delivering 70-220 MeV protons with fixed field in the superconducting magnets could reduce the cost and improve the adoption of proton therapy. While a number of magnet and cryogenics designs have been proposed, the combined capital and operating costs of state-of-the-art superconducting materials have not been analyzed. In response, we develop a thermoeconomic model of a multi-stage, conduction cooled gantry lattice and analyze the cryocooler operating cost, cryocooler capital cost and conductor capital cost for Nb-Ti, Nb_3Sn, REBCO and Bi-2223 over a continuous range of magnet temperatures, and a differential evolution algorithm is used to identify the optimal combination of thermal intercept temperatures. Although Nb_3Sn yields the lowest Net Present Value (NPV) of \$111.7k at a magnet temperature of 9.4 K, the optimized Bi-2223 design at 12.8 K approaches the realm of commercial feasibility by offering improved thermal stability and forgoing the need for costly conductor heat treatment and magnet quench training. Furthermore, it was found that Nb_3Sn was more cost effective than Nb-Ti and that REBCO was not economically viable for the parameters of this investigation. The thermoeconomic model developed herein can optimize conductor choices, magnet temperatures and thermal staging which has value for any conduction-cooled superconducting magnet.

Keywords: Proton therapy, superconducting magnet, thermoeconomics, cryocooler, REBCO, BSCCO, Nb3Sn

1. Introduction

Ion therapy utilizes the Bragg peak to ionize tissue volumes within a cancerous tumor. To improve the spatial resolution of treatment, state-of-the-art centers typically deliver protons from a rotating gantry. In an effort to reduce the cost of rotating gantries, which can facilitate the widespread adoption of both proton and carbon therapy [1], research efforts have focused on developing compact, high field superconducting gantry magnets [2, 3]. The fast magnetic field ramps associated with tumor scanning is a key challenge for the adoption of superconducting gantry magnets, and this concern has been exacerbated by trends toward faster treatment modalities such as breath-hold scanning and ultra-fast FLASH treatment [4].

Brouwer *et al* (2019) [5] developed a new magnet and optics solution with full momentum acceptance; 70-220 MeV proton beams are transmitted with the superconducting magnet system at fixed field. As illustrated in Fig. 1, accelerated protons exit a cyclotron and are bent onto a rotating gantry, where an energy degrader adjusts the treatment beam energy. The beam enters the side of two dipole magnets in a double bend achromat, forming a symmetric optics system where protons are delivered to a fixed location regardless of beam energy. The three beam energies illustrated in yellow, pink and purple show higher energy particles penetrating deeper into the magnet. A quadrupole triplet is included before and after the superconducting (SC) bending section to meet clinical requirements on beam spot size and shape at the patient location (isocenter).

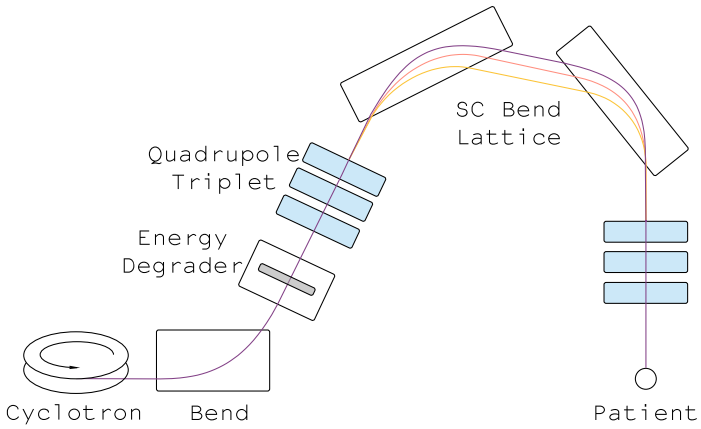

Figure 1: Overview of fixed-field gantry layout proposed in Ref. [5]. Low energy protons shown in yellow, high energy protons shown in purple.

Realizing the opportunity of a fixed-field superconducting gantry with racetrack dipoles, a Varian-led study explored trade-offs in operating temperature, field strength, conductor performance and conductor cost for proton therapy and reported Bi-2223 tapes as a promising conductor for the application [6]. The results of Ref. [6] motivate a quantitative cost analysis of the superconducting magnet system for the fixed-field gantry in Brouwer

et al (2019) [5]. To balance competing objectives of conductor and cryogenics costs, a thermoeconomic model is required to convert capital and operating costs into a Net Present Value (NPV [$]) or cost rate ([$/hr]).

A number of magnet cost evaluations have been reported in literature. Green and Strauss have extensively investigated the costs of superconducting magnets [7] and cryogenic refrigeration [8] with an emphasis on large-scale and liquid-helium cooled systems. Oomen *et al* (2000) [9] explored the impact of AC losses in Bi-2223 tapes on the economic viability of superconducting transformers and motors as a function of operating temperature. Jeong and Kim (2010) investigated the anchoring temperature of resistive current leads that minimized cryocooler work consumption [10]. Chang *et al* (2002) [11] investigated the cryocooler work consumption as a function of the intercept temperature in a two-stage, conduction cooled superconducting magnet. Bjørk *et al* (2016) [12] compared the conductor capital, cryocooler capital and cryocooler operating costs of a REBCO magnet to a permanent magnet Halbach array with a single stage of cooling at 77 K. Teyber and Rowe (2019) [13] presented a system-level cost optimization of an Active Magnetic Regenerative Liquefier (AMRL); with a REBCO solenoid and a single cooling stage, the combined capital and operating costs were found to decrease with operating temperature down to the lowest considered temperature of 10 K.

While these works touch on decades of magnet costing, a thermoeconomic analysis of superconducting materials, magnet temperatures and thermal staging has not been reported. In this work, we develop a thermoeconomic model of a multi-stage, conduction cooled magnet system and apply it to optimize conductor and cryogenics choices for the novel gantry layout in Ref. [5]. The lifetime gantry ownership costs are optimized with Nb-Ti, Nb_3Sn, REBCO and Bi-2223, and an emphasis is given to conductors that scale to higher fields. The impact of radiation shielding and thermal intercepts is explored, and a sensitivity analysis identifies pathways for further cost reductions.

2. Methods

The gantry design of Ref. [5] makes use of two superconducting magnets, and each magnet consists of racetracks in an iron yoke. To decouple the beam optics from the cost analysis, we consider the conductor cost required to achieve the 376 kA-turns over the 6.36 meter winding perimeter in each magnet. With a peak bore field of 3.5 T, the conductor is subjected to 4 T. For the thermal analysis, each magnet is approximated as a cylinder with a radius of 0.55m, a length of 1.2m and a mass of 2400kg (4,800kg total).

Table 1: Magnet parameters used in cost analysis [5].

Parameter	Value
Current per magnet [kA-turns]	376
Winding perimeter per magnet [m]	6.36
Peak field on conductor [T]	4
Mass per magnet [kg]	2400
Magnet length [m]	1.2
Effective diameter [m]	0.55

2.1. Thermoeconomic evaluation

Both capital and operating costs are required to deliver protons to a patient. Neglecting facility and structure costs, the capital investment consists of cryocoolers (Z_{cryo} [\$]) and superconducting material (Z_{cond} [\$]). In the absence of maintenance and institutional burdens, operating costs are evaluated as the product of electricity price and cryocooler work consumption ($c_{\text{elec}}\dot{W}$ [\$/hr]):

$$Z_{\text{gantry}} = Z_{\text{cryo}} + Z_{\text{cond}} + Z_{\text{elec}} \tag{1}$$

where Z_{elec} is evaluated as the Net Present Value (NPV) of hourly electrical costs compounded annually over the expected lifetime of $N = 20$ years at a discount rate $i_{\text{d}} = 0.02$, representative of inflation. The U.S. commercial electricity price of 0.10 \$/kWh is considered, and the leading factor of 8760 converts hourly costs into an annual payment.

$$Z_{\text{elec}} = \sum_{n=1}^{N} \frac{8760 c_{\text{elec}} \dot{W}}{(1+i_d)^n} \tag{2}$$

The thermoeconomic formulation can identify where competing objectives are balanced, minimizing the treatment cost of proton therapy. As the magnet temperature decreases, the superconductor critical current increases allowing the amount of conductor (and conductor cost) to decrease. A decreased magnet temperature requires more expensive cryocoolers and increased cryocooler work consumption.

2.2. Thermal model

The cryocooler work consumption ($\dot{W}$) and absolute capital cost (Z_{cryo}) are functions of the thermal loads, which are calculated from the multi-stage thermal model in Fig. 2. To reduce the refrigeration load at the cold stage, thermal intercepts are introduced with independent cryocoolers operating at intermediate temperatures (single intercept, T_{M}, shown in Fig. 2). This reduces the cryocooler operating costs at the expense of increased cryocooler capital costs. At each stage (T_i), the cooling load ($\dot{Q}_{\text{C},i}$) consists of thermal radiation ($\dot{Q}_{\text{rad},i}$), conduction through structural supports ($\dot{Q}_{\text{struc},i}$) and conduction through current leads ($\dot{Q}_{\text{lead},i}$) originating from the adjacent thermal reservoir (T_{i+1}). An additional Ohmic source term arises ($\dot{Q}_{\text{Ohm},i}$) when the local stage implements resistive current leads. An energy balance yields the required cooling power at each stage:

$$\dot{Q}_{\text{C},i} = \left(\dot{Q}_{\text{rad},i} + \dot{Q}_{\text{struc},i} + \dot{Q}_{\text{lead},i} + \dot{Q}_{\text{Ohm},i}\right) - \left(\dot{Q}_{\text{rad},i-1} + \dot{Q}_{\text{struc},i-1} + \dot{Q}_{\text{lead},i-1}\right) \tag{3}$$

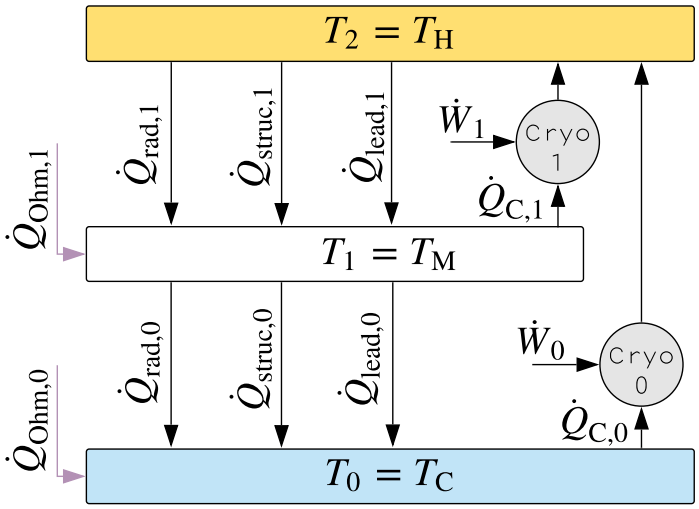

Figure 2: Overview of thermal model with a single intercept temperature (T_{M}).

2.3. Cryocoolers

A cryocooler removes heat ($\dot{Q}_{\mathrm{C},i}$) from each thermal reservoir (T_i) and rejects it to room temperature ($T_{\mathrm{H}} = 298$ K) while consuming work ($\dot{W}_i$). If the second law efficiency ($\eta_{II,i}$) is known *a priori*, the stage work consumption can be evaluated as:

$$\dot{W}_{\mathrm{i}} = \frac{\dot{Q}_{\mathrm{C},i}}{\eta_{II,i}} \frac{(T_H - T_i)}{T_i} \tag{4}$$

allowing the cryocooler work consumption to be written as a function of the thermal load. Eq. 4 demonstrates the high operating costs associated with low magnet temperatures; as the magnet temperature (T_{C}) decreases, the thermal load ($\dot{Q}_{\mathrm{cryo}}$) increases, the second law efficiency (η_{II}) decreases and Carnot scaling ($\Delta T/T_{\mathrm{C}}$) increases. It should be emphasized that thermodynamic efficiency is increased by providing cooling at intermediate stages; it is very expensive to remove heat from a 4.2 K source.

Second law efficiencies vary not only with temperature and cooling power, but with the operating state of any other stage in a cascaded system (e.g., two-stage Gifford-McMahon Cryocooler). As in Ref. [11] and as illustrated in Fig. 2, our analysis focuses solely on multiple installations of single-stage cryocoolers. This allows us to consider a second law efficiency (η_{II}) that increases linearly from 1% at 4.2 K to 10 % at 77 K and remains constant at 10 % for elevated temperatures (Eq. 5). This synthetic fit is motivated by the cryocooler survey of ter Brake *et al* (2002) [14], where η_{II} is assumed to be independent of cooling capacity at the small scales considered here.

$$\eta_{II,\mathrm{cryo}} = \begin{cases} 0.001236 T_i + 0.004807, & \text{if } T_i \leq 77 \\ 0.1 & \text{otherwise} \end{cases} \tag{5}$$

In addition to the operating costs of work consumption, the cryocooler capital cost (Z_{cryo}) must be quantified. To allow a continuous parameterization of operating temperature, two synthetic cryocoolers are considered with properties inspired from industry. The first cryocooler model (so-called High Temperature (HT) cryocooler) has a load curve ($\dot{Q}_{\mathrm{cap}}(T_i)$) interpolated from a commercial single-stage cryocooler with a quiescent no-load temperature of 12.6 K. The second cryocooler model (so-called Low Temperature (LT) cryocooler) implements the load curve fit in Ref. [15] for a PT415 with an unloaded first stage (i.e., providing cooling only at a single temperature). The curve fit for both cryocoolers cooling capacity is shown in Eq. 6 with the parameters in Table 2.

$$\dot{Q}_{\mathrm{cap},i} = a + bT_i + cT_i^2 + dT_i^3 + eT_i^4 \tag{6}$$

The unit capital costs of the synthetic high and low temperature cryocoolers are \$15,000 and \$40,000, respectively, and the total capital costs (Z_{cryo}) are evaluated from the integer number of cryocoolers required to meet the cooling load of each stage ($\lceil \dot{Q}_{\mathrm{C},i}/\dot{Q}_{\mathrm{cap}} \rceil$). In every cost evaluation, both cryocooler models are considered and the most cost effective

Table 2: Cryocooler cooling power fits (Eq. 6) for synthetic High Temperature (HT) and Low Temperature (LT) cryocoolers. Minimum and maximum bounds for the fits are shown.

Parameter	HT cryocooler	LT cryocooler
a	-57.0283	-5.2590
b	4.7243	1.4738
c	-0.01479	-8.8986e-3
d	-5.6947e-05	5.2029e-5
e	3.1640e-07	-1.3019e-7
Min Temp. [K]	12.6	4.2
Max Temp. [K]	165	200

option is selected. In addition to the cryocooler pricing and treatment of second law efficiency, the cryocooler treatment is synthetic in the assumption that any thermal load can be isothermally refrigerated up to the cryocoolers cooling capacity. In reality, this would be accomplished by selecting a smaller cryocooler with a reduced cooling power. Finally, it should be mentioned that performance degradation from cryocooler rotation or stray magnetic fields is not considered.

2.3.1. Thermal radiation Due to the large variance in cryogenic thermal loads, two methods are employed to model radiation heat transfer. The first approach considers thermal stages wrapped in copper shields ($\dot{Q}^{\text{copper}}_{\text{rad},i}$), which is a high heat load scenario. The second approach considers stages wrapped in Multi-Layer Insulation ($\dot{Q}^{\text{MLI}}_{\text{rad,i}}$), where low emissivity sheets are separated by low conductivity material; this represents a low heat load scenario. For both techniques, the heat transfer area of the cold stage (T_{C}) is defined by the magnet parameters in Table 1, and a 150mm annular and longitudinal spacing is assumed between subsequent stages.

For the high heat load scenario ($\dot{Q}^{\text{copper}}_{\text{rad},i}$), electromagnetic radiation is approximated as:

$$\dot{Q}^{\text{copper}}_{\text{rad},i} = F_{\epsilon,i}\sigma A_i(T^4_{i+1} - T^4_i) \tag{7}$$

where $\dot{Q}^{\text{copper}}_{\text{rad},i}$ is the radiation heat load refrigerated by the stage's cryocooler, A_i is the heat transfer area of the cooling stage's inner surface (e.g., magnet for i=0), σ is the Stefan-Boltzmann constant and $F_{\epsilon,i}$ is the combined emissivity for nested concentric cylinders:

$$F_{\epsilon,i} = \Big(\frac{1}{\epsilon_i} + \frac{A_i}{A_{i+1}}\big(\frac{1}{\epsilon_{i+1} - 1}\big)\Big)^{-1} \tag{8}$$

where the emissivity is linearly interpolated between values of 0.02, 0.06 and 0.1 at temperatures of 4 K, 80 K and 300 K [16].

For the low heat load scenario, we consider the Lockheed equation [17] for MLI:

$$\dot{Q}^{\text{MLI}}_{\text{rad,i}} = \frac{A_i}{\text{n}_{\text{MLI}}}\Big(c_{\text{cond}}N^{2.56}_{*}\frac{(T_{i+1} + T_i)}{2}(T_{i+1} - T_i) + c_{\text{rad}}\epsilon_0(T^{4.67}_{i+1} - T^{4.67}_i)\Big) \tag{9}$$

where $c_{\text{cond}} = 8.95\text{x}10^{-8}$, $c_{\text{rad}} = 5.39\text{x}10^{-10}$, N_* is the layer density (19 layers/cm) and n_{MLI} is the total number of layers (10). The values for N_* and n_{MLI} are based on the European XFEL [18], and the 4.67 in Eq. 9 accounts for a $T^{0.67}$ scaling of emissivity from a room temperature value of $\epsilon_0 = 0.04$. Note that Eq. 9 does not consider the combined emissivity or the outer cylinder geometry.

2.3.2. Structural supports The rotating gantry magnet must be supported in all orientations. A simple and conservative approach is taken to model the conductive heat leaks through G10 structural supports, where the top strut suspends the entire magnet mass (2400kg per magnet) in tension. The cross sectional area of the strut is then chosen so that the link sustains 225 MPa in tension (50% of tensile strength, σ_{ultimate}, with fibers aligned in tension). The leading factor of 6 accounts for the supports in each orientation.

$$A^{\text{tot}}_{\text{struc}} = 6n_{\text{magnets}}\frac{m_{\text{magnet}}\text{g}}{0.5\sigma_{\text{ultimate}}} \tag{10}$$

The total cross sectional area, $A^{\text{tot}}_{\text{struc}}$, is then used to evaluate the structural conductive heat leak with the temperature-dependent thermal conductivity evaluated along the fiber orientation:

$$\dot{Q}_{\mathrm{struc},i} = \frac{A^{\mathrm{tot}}_{\mathrm{struc}}}{L_{\mathrm{struc},i}} \int_{T_i}^{T_{i+1}} k_{G10}(T) dT \tag{11}$$

where L_{struc} is evaluated as the radial length between concentric cylinders (150mm), T_i is the local cryocooler stage and T_{i+1} is the adjacent warm thermal reservoir. In the stage energy balance (Eq. 3), $\dot{Q}_{\mathrm{struc},i-1}$ is evaluated from Eq. 11; conduction from structural supports reduces the heat load of the adjacent warm cryocooler (see Fig. 2). Although straight, radial supports are considered here, it should be noted that conduction heat leaks can be reduced with long, angled G10 magnet supports.

2.3.3. Current leads Current leads introduce a significant heat leak that must be minimized when designing a conduction cooled magnet. For multi-stage systems, resistive current leads are typically used in the warm stages, resulting in both heat conduction ($\dot{Q}_{\mathrm{lead},i}$) from the hot thermal reservoir and Ohmic heating ($\dot{Q}_{\,\mathrm{Ohm},i}$) from the resistive leads that must be refrigerated by a stage's cryocooler. Furuse *et al* (2009) [19] derived the current lead temperature distribution with an Ohmic source term, and presented the optimal conductor aspect ratio (ζ_{lead}) that balances Ohmic power dissipation with axial heat conduction:

$$\zeta_{lead} = \frac{l_{\mathrm{lead}}}{A_{\mathrm{lead}}} = \frac{\bar{k}_a}{I\sqrt{L_a}}\cos^{-1}\Big(\frac{T_i}{T_{i+1}}\Big) \tag{12}$$

where $\bar{k}_a$ is the integrated average thermal conductivity, I is the coil current and L_a is the average Lorenz number. The Lorenz number is assumed to follow the Wiedemann-Franz law and is assigned a value of 2.45 x 10^{-8} WΩK^{-2}. As shown in Fig. 2, the stage energy balance must consider both inflows and outflows of energy; it can be shown that no heat transfers from the hot stage into the resistive current lead when the optimal aspect ratio (Eq. 12) is used ($dT/dx|_{x=0} = 0$). This implies that $\dot{Q}_{\mathrm{lead},i-1} = 0$ in the stage energy balance (Eq. 3), and the original expression reported by Furuse *et al* (2009) [19] can be considered for the combined Ohmic heating and conduction losses in resistive current leads:

$$\dot{Q}_{\mathrm{lead},i} + \dot{Q}_{\mathrm{Ohm},i} = n_{\mathrm{lead}}\mathrm{I}\sqrt{L_a(T_{i+1}^2 - T_i^2)} \tag{13}$$

where $n_{\mathrm{lead}} = 2$ is the number of external current leads (assumed that all coils are connected in series to reduce heat leaks). For a resistive lead between 77 K and 298 K, the combined heat leak is on the order of 90 W/kA, emphasizing the importance of low current conductors (in contrast to superconducting cables) and intermediate cooling.

For cases with one or more thermal intercepts, Ohmic heating can be eliminated from colder stages by implementing high temperature superconducting leads ($\dot{Q}_{\mathrm{Ohm},i} = 0$). Here we consider a stack of low thermal conductivity Bi-2223 tapes (Sumitomo DI-BSCCO type G). The bulk thermal conductivity is a strong function of temperature, requiring the heat leak to be integrated as:

$$\dot{Q}_{\mathrm{lead},i} = \frac{n_{\mathrm{lead}}n_{\mathrm{tapes}}A_{\mathrm{tape}}}{L_{\mathrm{lead}}}\int_{T_i}^{T_{i+1}} k(T)dT \tag{14}$$

where the temperature dependent thermal conductivity ($k(T)$) is evaluated from the Sumitomo product literature, $n_{\mathrm{lead}} = 2$ (assumed that all coils are connected in series), $A_{\mathrm{tape}} = 1.4\mathrm{mm}^2$ for a single Bi-2223 tape, T_i is the local cold temperature and T_{i+1} is the adjacent warm thermal reservoir. To minimize conductive heat leaks, the current lead is assumed to follow a meandered path between stages with a fixed length of $L_{\mathrm{lead}} = 1\mathrm{m}$. The individual tape current is used to evaluate the integer number of tapes in the tape stack (n_{tapes}). The critical current ($I_{\mathrm{c}}(B,T)$) is evaluated at the local warm stage temperature (T_{i+1}) and 0.2 T; the ferromagnetic flux return path in the magnet design minimizes stray

magnetic field. To minimize power-law losses (small resistive voltage in the flux-flow regime), tape currents are constrained below 80 % of the critical current. It should be emphasized that when resistive current leads are used with an optimal aspect ratio, $\dot{Q}_{\mathrm{lead},i-1} = 0$ in the stage energy balance (Eq. 3). When a superconducting current lead is used, the conduction heat leak is drawn from the adjacent warm stage, and $\dot{Q}_{\mathrm{lead},i-1}$ in Eq. 3 is evaluated from Eq. 14.

2.4. Conductor cost

The conductor and cryogenics cost analysis is decoupled from the beam dynamics and magnet design by considering the amount of conductor required to obtain 376 kA-turns over the 6.36 meter winding perimeter of each magnet, evaluated with 4 T on the conductor. For anistropic conductors, it is assumed that the magnetic field is aligned in the worst orientation. Although Nb-Ti is briefly considered in the manuscript, we focus on Nb_3Sn, REBCO and Bi-2223 due to the wide range of operating temperatures and ability to scale to higher field designs (e.g., carbon therapy). In this section, the methodology for evaluating conductor costs (Z_{cond}) is presented.

The temperature-dependent Nb_3Sn critical current is evaluated with the Godeke relation [20] using OST-type II internal tin conductor [21]. The REBCO SCS-4050 critical current surface ($I_{\mathrm{c}}(B,\, T\,)$) is interpolated from Zhang *et al* (2014) [22], and the 4mm tape width is considered to achieve a comparable operating current with the Nb_3Sn and Bi-2223 conductors. The Bi-2223 critical current surface is interpolated from the Sumitomo HT-SS (DI-BSCCO) product documentation. The stainless steel reinforced tape (HT-SS) is considered due to its reduced cost and compatibility with the bend diameter of the main racetrack coils in the referenced design, however high field applications (e.g., carbon therapy) or small bend radii coils may favor the stronger HT-NX conductor. The Bi-2223 tapes have a cross section of 4.5 x 0.3mm, which is presently the only commercially available width.

For all three conductors, the magnet current is evaluated at 80 % of the critical current. This safety margin reflects the importance of thermal stability in proton gantries; a magnet quench is highly undesired during treatment. Furthermore, this safety factor reduces power-law losses in HTS materials that add to the cryocooler heat load.

The Bi-2223 conductor is assumed to cost \$20/m for the Sumitomo HT-SS 4.5 x 0.31mm tape, and this cost is not anticipated to decrease in the near future. While the SuperPower SCS-4050 REBCO tape can cost as high as \$100/m, we use a value of \$40/m for the 4.0 x 0.1mm tape. Cooley *et al* (2005) [23] and Vostner *et al* (2017) [24] reported costs for internal tin Nb_3Sn. Following these works, a cost of \$3.5/m is considered for a 0.81mm diameter strand. Although internal tin Nb_3Sn is considered here, Ref. [24] reports a 10% cost reduction with bronze route processing.

The critical current (I_{c}), conductor cost-per-meter, (c_{cond}), winding perimeter (P_{magnet}), and total current can then be used to evaluate the conductor capital cost, Z_{cond}, with the parameters in Table 1:

$$Z_{\mathrm{cond}} = n_{\mathrm{magnets}} c_{\mathrm{cond}} P_{\mathrm{magnet}} \frac{I_{\mathrm{tot}}}{I_{\mathrm{c}}} \tag{15}$$

3. Results

3.1. Single thermal intercept

The total superconducting magnet cost over a 20 year lifetime is shown in Fig. 3 and Fig. 4 for the high heat load ($\dot{Q}_{\mathrm{rad},i}^{\mathrm{copper}}$, Eq. 7) and low heat load ($\dot{Q}_{\mathrm{rad,i}}^{\mathrm{MLI}}$, Eq. 9) scenarios, respectively, with a single thermal intercept. Contours are presented as a function of the magnet temperature (T_{C}) and thermal intercept temperature (T_{M}) for Nb_3Sn (top), REBCO (middle) and Bi-2223 (bottom) with contours ranging from \$100k to \$550k in \$25k increments. In both heat load scenarios, Nb_3Sn is the lowest cost conductor followed closely by Bi-2223. REBCO costs several times more than the other conductors. The lowest cost point is indicated with a small white circle, and the corresponding system properties are summarized in Table 3.

For Nb_3Sn in the high heat load case of Fig. 3, the minimum cost of \$179.5k occurs at T_{C} = 10.2 K and T_{M} = 83.2 K. When the insulation is improved, as in Fig. 4, the total cost of Nb_3Sn decreases to \$111.7k at T_{C} = 9.4 K and T_{M} = 76 K; by improving the radiation shielding between layers with MLI, the lifetime ownership cost is decreased by\$67.8k. These magnet temperatures are higher than many conduction cooled Nb_3Sn systems, demonstrating that for the parameters of this investigation, increased conductor costs are offset by decreased operating costs at elevated magnet temperatures. As shown in Table 3, MLI has the greatest effect on the warmer layers, allowing the thermal intercept temperature to decrease from 83.2 K to 76.3 K.

With REBCO in the high heat load case of Fig. 3, the cryogenics costs are overwhelmed by conductor capital and the minimum cost of \$497.5k is found at T_{C} = 5.6 K and T_{M} = 77 K. With MLI radiation shielding, the total cost decreases to \$414k at T_{C} = 5.7 K and T_{M} = 70.9 K as shown in Fig. 4. The competing cost elements play a more equal role with Bi-2223, and the minimum cost of \$276.5k is obtained at T_{C} = 12.8 K and T_{M} = 83.1 K for the high heat load case of Fig. 3. When the thermal insulation is improved, as in Fig. 4, the cost is reduced by \$80.8k to \$195.7k at T_{C} = 12.8 K and T_{M} = 78.3 K. In both heat load scenarios, the optimal Bi-2223 magnet temperature straddles the minimum operating temperature of the lower-cost, high temperature cryocooler (see Table 2). This cryocooler tradeoff point creates a discontinuity in all of the total cost contours that manifests as a vertical line at T_{C} = 12.8 K. A second discontinuity is observed near T_{M} = 83 K, where the critical current of the Bi-2223 current lead becomes inadequate and the model implements resistive current leads instead (Eq. 13).

Fig. 5 and Fig. 6 show the contributions of the electrical cost (top), conductor cost (middle) and cryocooler capital cost (bottom) to the total Bi-2223 superconducting gantry magnet cost for the high heat load and low heat load scenarios, respectively; Fig. 3 and Fig. 4 are the superposition of these three contours (Eq. 1). The electrical operating and cryocooler capital costs are sensitive to design choices; small changes in thermal reservoir temperatures can yield large changes in cost. Although the electrical operating and cryocooler capital costs

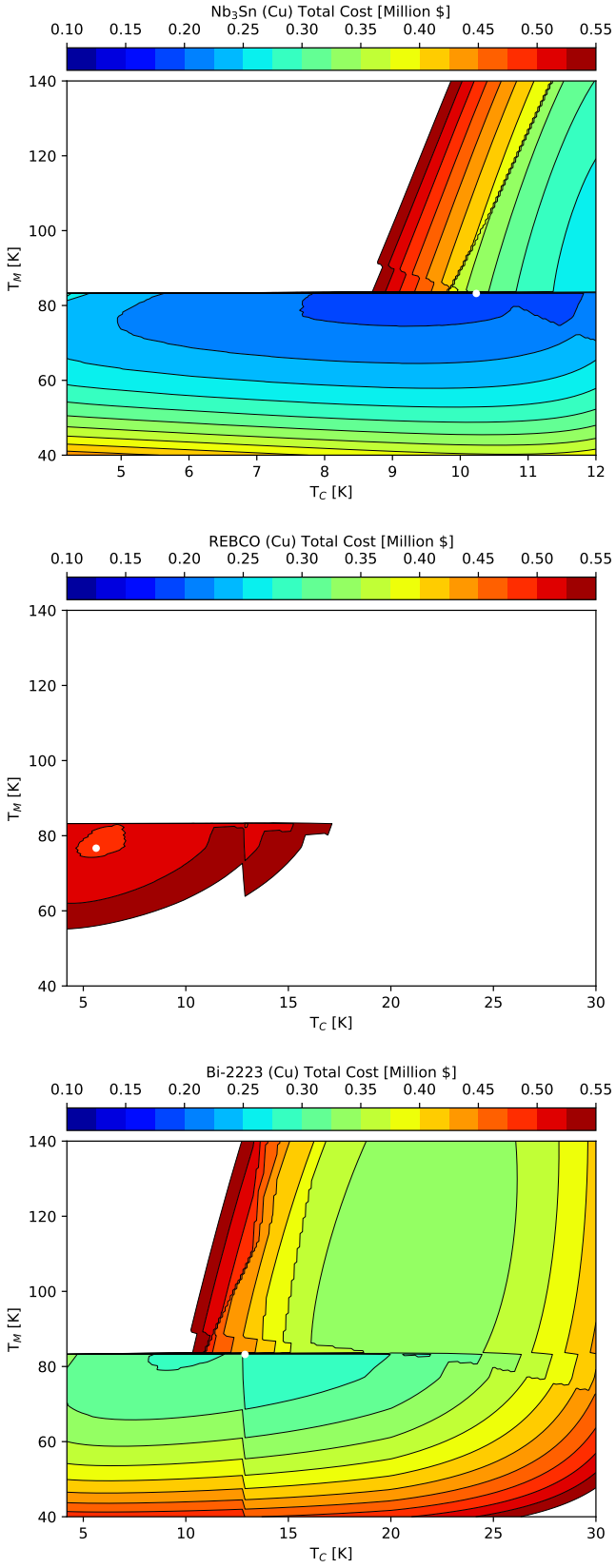

Figure 3: Contours of total cost as a function of magnet temperature (T_{C}) and thermal intercept temperature (T_{M}) for Nb_3Sn (top), REBCO (middle) and Bi-2223 (bottom) for the high heat load scenario ($\dot{Q}^{\mathrm{copper}}_{\mathrm{rad},i}$, Eq. 7). The lowest cost point is indicated with a small white circle, and the corresponding system properties are summarized in Table 3.

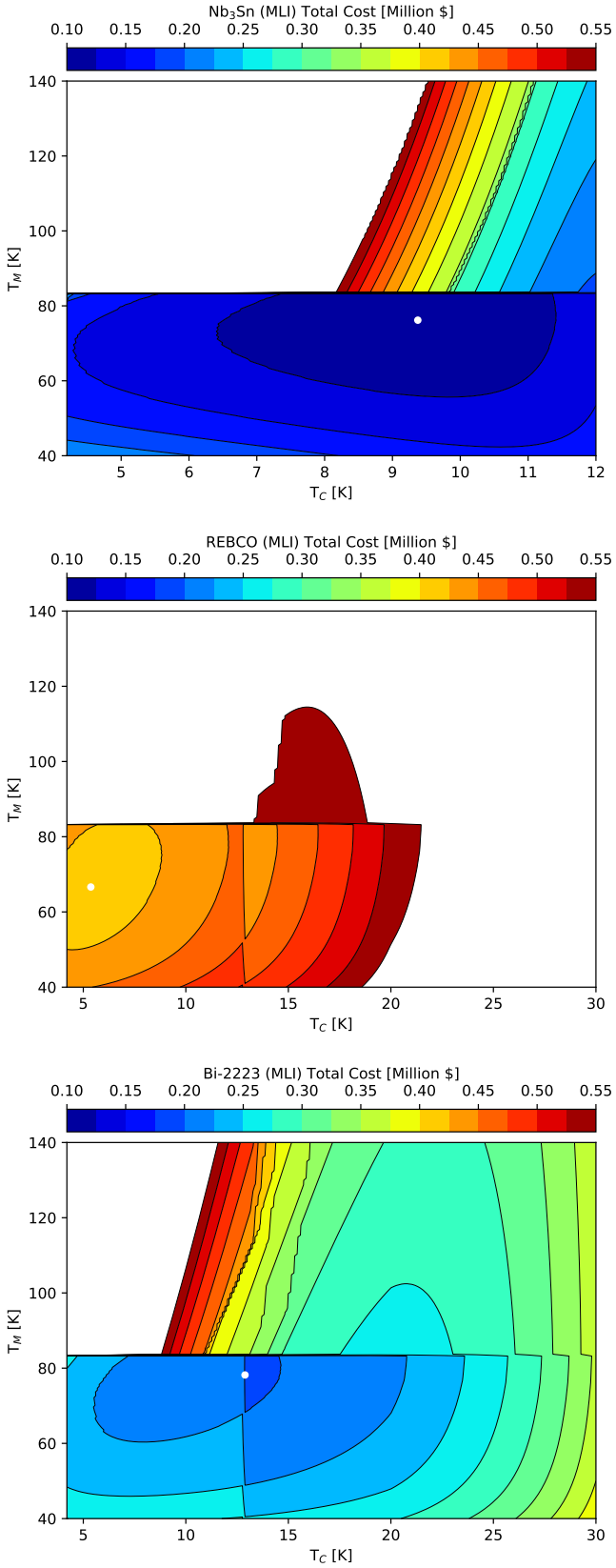

Figure 4: Contours of total cost as a function of magnet temperature (T_{C}) and thermal intercept temperature (T_{M}) for Nb_3Sn (top), REBCO (middle) and Bi-2223 (bottom) for the low heat load scenario ($\dot{Q}^{\mathrm{MLI}}_{\mathrm{rad,i}}$, Eq. 9). The lowest cost point is indicated with a small white circle, and the corresponding system properties are summarized in Table 3.

reduce with increasing T_C and T_M (top right corner of figures), with judicious thermal choices it is possible to achieve acceptable costs (i.e., lowest contour range) with T_C in the vicinity of 10-15 K. The irregular contour lines in the bottom of Fig. 5 and Fig. 6 reflect the discrete nature of the cryocooler capital cost treatment, where an integer number of cryocoolers is considered. Finally, the conductor cost is a function of the cold mass temperature (T_C) only.

Table 3: System parameters with optimized thermal reservoirs for the high heat load (Eq. 7) and low heat load (Eq. 9) scenarios with a single thermal intercept.

	Nb_3Sn (Eq. 7)	REBCO (Eq. 7)	Bi-2223 (Eq. 7)	Nb_3Sn (Eq. 9)	REBCO (Eq. 9)	Bi-2223 (Eq. 9)
$T_{C,0}$ [K]	10.21	5.59	12.82	9.42	5.71	12.82
$T_{M,1}$ [K]	83.22	76.98	83.13	76.30	70.87	78.26
$T_{H,2}$ [K]	298	298	298	298	298	298
I [A]	272.7	307.2	344.4	341.2	306.3	344.4
J_{eng} [A/mm^2]	529.1	768.0	246.8	662.1	765.0	246.8
Tot. L_{cond} [km]	8.80	7.81	6.97	7.03	7.83	6.97
$\dot{Q}_{rad,0}$ [W]	0.273	0.181	0.285	0.255	0.221	0.266
$\dot{Q}_{rad,1}$ [W]	190.91	186.08	190.88	14.03	14.10	14.00
$\dot{Q}_{lead,0}$ [W]	0.148	0.076	0.177	0.074	0.033	0.094
$\dot{Q}_{lead,1}$ [W]	24.43	27.69	30.85	30.77	27.76	31.00
$\dot{Q}_{struc,0}$ [W]	0.177	0.161	0.174	0.155	0.142	0.157
$\dot{Q}_{struc,1}$ [W]	1.16	1.19	1.16	1.19	1.20	1.18
$\dot{Q}_{C,0}$ [W]	0.598	0.418	0.635	0.484	0.396	0.517
$\dot{Q}_{C,1}$ [W]	216.05	214.61	222.44	45.57	42.69	45.76
$\dot{W}_0$ [W]	967.5	1867.4	684.0	901.1	1709.1	556.9
$\dot{W}_1$ [W]	5576.1	6163.5	5749.4	1335.6	1480.5	1284.9
Cryo. cap [k$]	55	70	45	55	55	30
Cond. cap [k$]	30.8	312.4	139.4	24.6	313.3	139.4
Elec. NPV [k$]	93.7	115.0	92.2	32.0	45.7	26.4
Total Cost [k$]	179.5	497.5	276.5	111.7	414.0	195.7
Total Cost [$/hr]	1.253	3.473	1.930	0.780	2.890	1.366

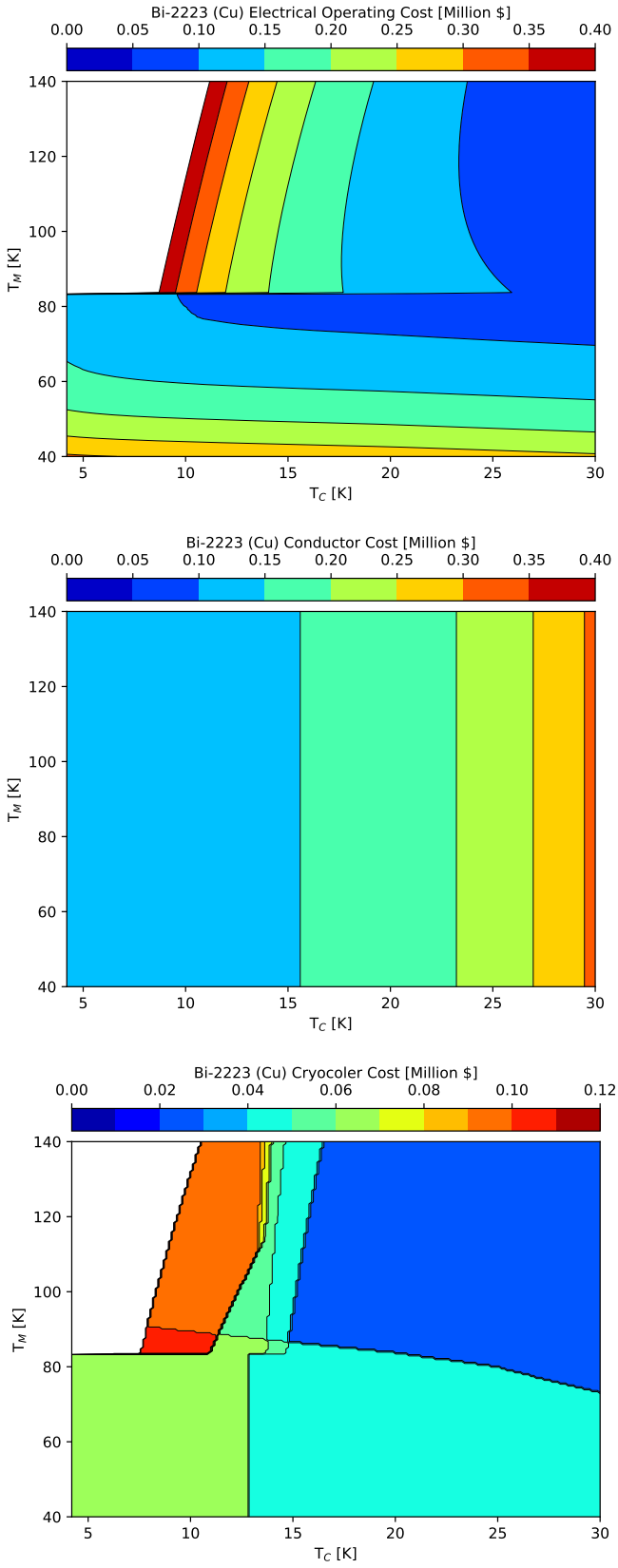

Figure 5: Contours of electrical net present cost (top), conductor cost (middle) and cryocooler capital cost (bottom) for Bi-2223 as a function of magnet temperature (T_{C}) and thermal intercept temperature (T_{M}) for the high heat load scenario ($\dot{Q}_{\mathrm{rad},i}^{\mathrm{copper}}$, Eq. 7).

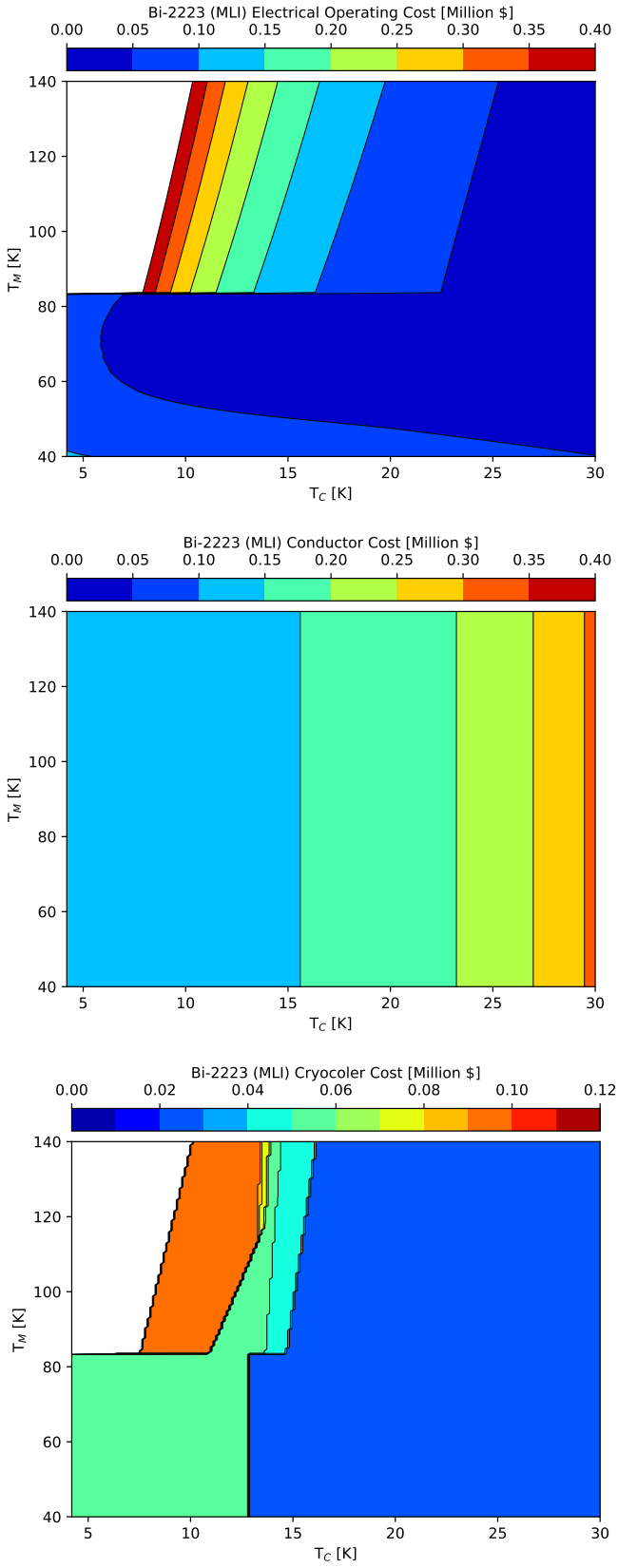

Figure 6: Contours of electrical net present cost (top), conductor cost (middle) and cryocooler capital cost (bottom) for Bi-2223 as a function of magnet temperature (T_{C}) and thermal intercept temperature (T_{M}) for the low heat load scenario ($\dot{Q}^{\mathrm{MLI}}_{\mathrm{rad,i}}$, Eq. 9).

3.2. Multiple thermal intercepts

In this section, the impact of multiple cooling stages on lifetime cost is explored. The results in Fig. 3 and Fig. 4 demonstrate the importance of thermal insulation, and we focus here on the low heat load case with MLI wrapped stages ($\dot{Q}^{\mathrm{MLI}}_{\mathrm{rad,i}}$, Eq. 9). As cost contours can no longer be presented with multiple intercept temperatures, the problem is reformulated as a minimization at each magnet temperature. For $n_{\mathrm{intercept}}$ thermal intercepts, this is expressed as:

$$\mathrm{Min}\ Z_{\mathrm{gantry}}(T_{\mathrm{M},1}, ..., T_{\mathrm{M},n_{\mathrm{intercept}}})|_{T_{\mathrm{C}}=const} \tag{16}$$

and solved with a parallel differential evolution algorithm [25]. Initial prototyping of multi-stage cooling revealed optimal interface temperatures converging above the operating ranges of the high and low temperature cryocoolers (see Table 2). In response, a third synthetic cooler is added to the analysis with properties inspired from a commercial R452A single-stage refrigerator. A linear cooling power fit is applied to the product documentation, $\dot{Q}_{\mathrm{cap},i} = -4312 + 19.1T_i$, yielding cooling powers of 100 W at 231 K and 400 W at 246.5 K. A constant second law efficiency of $\eta_{II,\mathrm{chiller}} = 0.2$ and unit capital cost of \$7,500 are considered based on the product documentation. The thermoeconomic model evaluates the three coolers at each thermal stage, and the lowest cost (capital and operating) option is selected.

The total cost as a function of T_{C} is shown in Fig. 7 for Nb_3Sn with one (top), two (middle) and three (bottom) thermal intercepts. Similar plots are shown for REBCO and Bi-2223 in Fig. 8 and Fig. 9, respectively, with horizontal lines in \$100k increments to facilitate comparison between the different superconductors. The total cost is presented as a stack plot showing the optimized contributions of electrical operating (red), conductor capital (light blue) and cryocooler capital (dark blue) costs. The costs are further broken down into the contribution from each stage, where labeling is consistent with Fig. 2. The detailed parameters are shown in Table 4 for the lowest cost points of Fig. 7 and Fig. 9 for Nb_3Sn and Bi-2223 with one, two and three thermal intercepts. As the REBCO configurations cost several times more than the Nb_3Sn and Bi-2223 magnets, the results are not tabulated.

Focusing first on Nb_3Sn in Fig. 7, the minimum total cost increases from \$111.7k with a single thermal intercept to \$112.4k and \$116.1k with two and three intercepts, respectively. Similar behavior is also observed with Bi-2223 (Fig. 9), however the addition of a second cooling stage results in a marginal cost reduction for REBCO (Fig. 8). This demonstrates that the decreased electrical operating costs with an additional cooling stage do not justify the increased capital cost of an additional cooler for the thermal loads of this analysis.

As more thermal intercepts are added, operating costs become less sensitive to magnet temperature. This is especially prevalent with Nb_3Sn in Fig. 7, where the operating costs constitute a significant portion of the total cost. This behavior is difficult to observe with REBCO in Fig. 8; the conductor-dominated cost suggests that ultra-high heat loads (e.g., thermonuclear fusion) are required to commercially justify REBCO operation at elevated

temperatures.

Readers should take note of the operating currents in Table 3 and Table 4 for the different conductors and cryogenics configurations explored throughout this work. In particular, the total current lead heat leak ($\sum \dot{Q}_{\text{lead},i}$) is found to increase with the number of thermal stages. This is a result of the nonlinear thermal reservoir dependence in Eq. 13, where it may not be cost effective to anchor resistive current leads at every thermal stage. Future work will consider this in the optimization, and the reader is directed to Refs. [10, 19] for more information on resistive current leads.

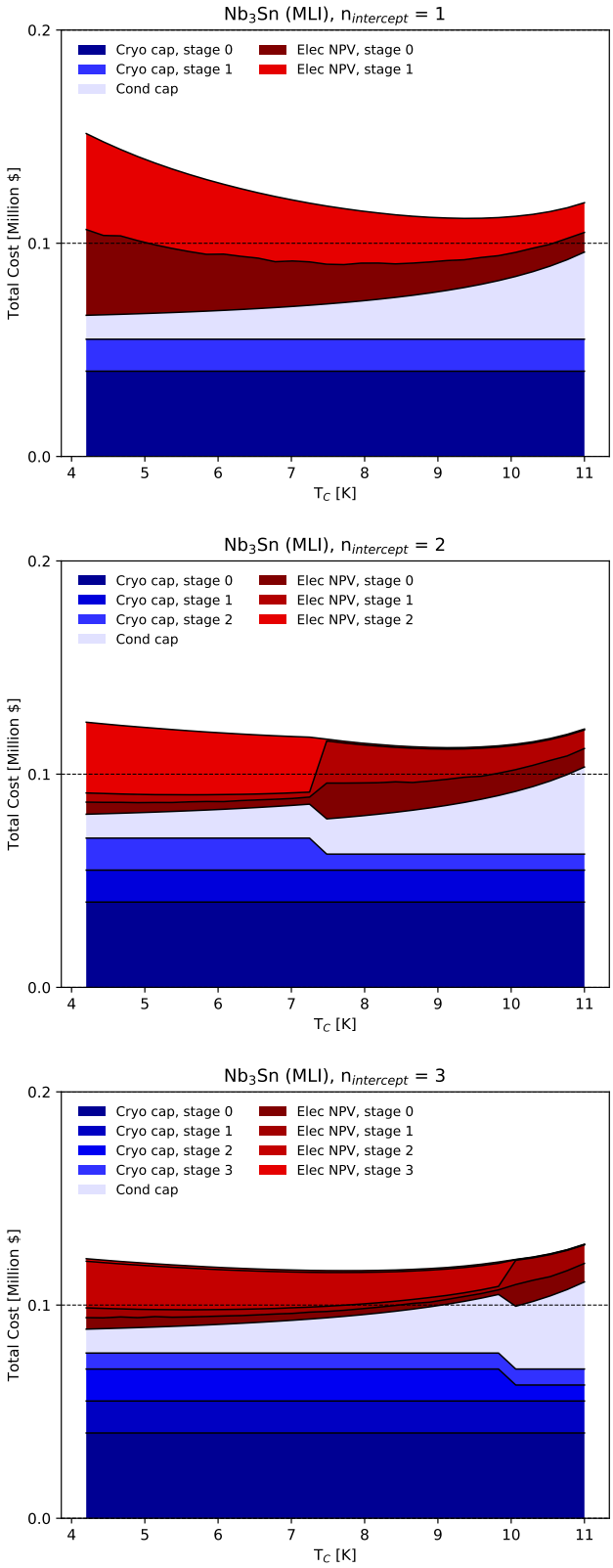

Figure 7: Optimal composition of cost as a function of T_{C} for Nb_3Sn with one (top), two (middle) and three (bottom) thermal intercepts for the low heat load scenario ($\dot{Q}^{\mathrm{MLI}}_{\mathrm{rad,i}}$, Eq. 9).

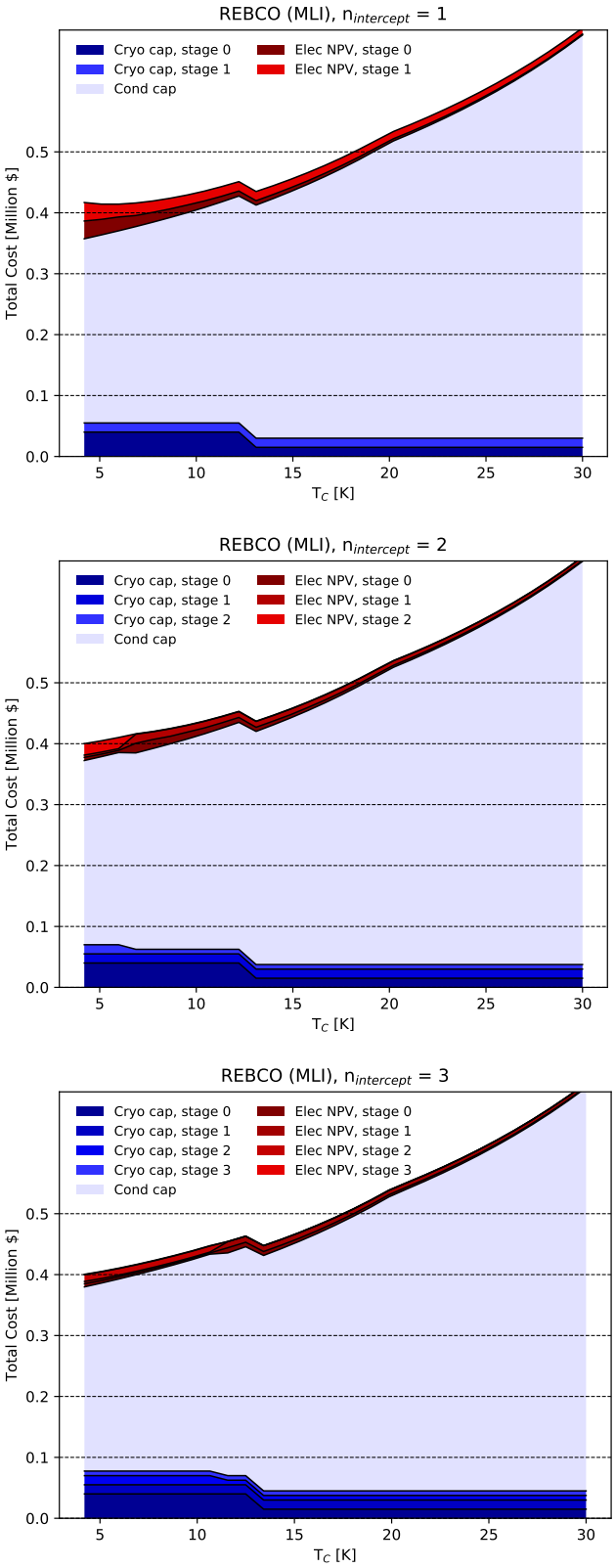

Figure 8: Optimal composition of cost as a function of T_{C} for REBCO with one (top), two (middle) and three (bottom) thermal intercepts for the low heat load scenario ($\dot{Q}_{\mathrm{rad,i}}^{\mathrm{MLI}}$, Eq. 9).

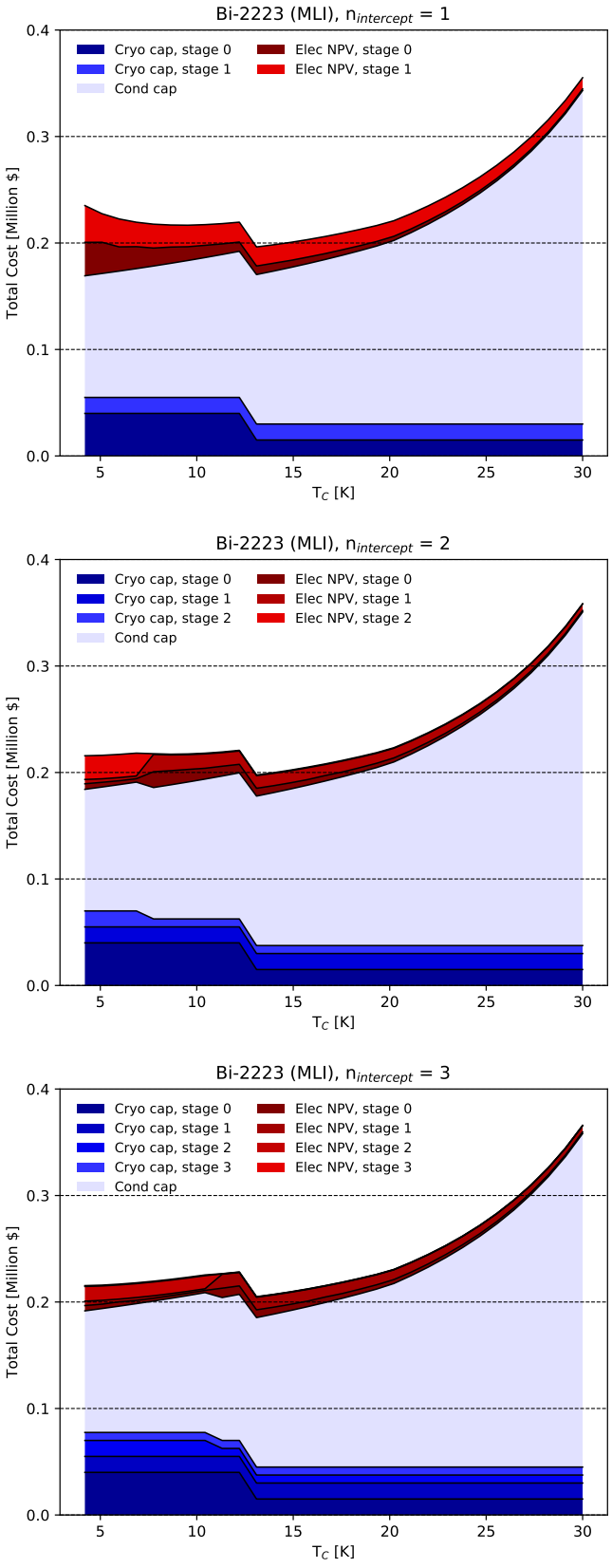

Figure 9: Optimal composition of cost as a function of T_{C} for Bi-2223 with one (top), two (middle) and three (bottom) thermal intercepts for the low heat load scenario ($\dot{Q}^{\mathrm{MLI}}_{\mathrm{rad,i}}$, Eq. 9).

Table 4: System parameters with optimized results for Nb_3Sn and Bi-2223 with 1, 2 and 3 thermal intercepts. All results generated with the low heat load scenario ($\dot{Q}^{\mathrm{MLI}}_{\mathrm{rad,i}}$, Eq. 9), and REBCO is not included due to its significantly higher cost.

	Nb_3Sn 1	Nb_3Sn 2	Nb_3Sn 3	Bi-2223 1	Bi-2223 2	Bi-2223 3
$T_{\mathrm{C},0}$ [K]	9.42	9.2	7.8	12.82	12.82	12.82
$T_{\mathrm{M},1}$ [K]	76.3	73.53	30.39	78.26	77	77.03
$T_{\mathrm{M},2}$ [K]	ø	227.29	83.15	ø	227.24	226.62
$T_{\mathrm{M},3}$ [K]	ø	ø	227.88	ø	ø	268.85
$T_{\mathrm{H},2}$ [K]	298	298	298	298	298	298
I [A]	341.2	360.3	481.6	344.4	344.4	344.4
J_{eng} [A/mm^2]	662.1	699.2	934.6	246.9	246.9	246.9
Tot. L_{cond} [km]	7.03	6.66	4.98	6.97	6.97	6.97
$\dot{Q}_{\mathrm{rad},0}$ [W]	0.255	0.236	0.037	0.266	0.257	0.257
$\dot{Q}_{\mathrm{rad},1}$ [W]	14.028	5.784	0.499	14.002	5.736	28.962
$\dot{Q}_{\mathrm{rad},2}$ [W]	ø	13.071	9.002	ø	13.077	16.086
$\dot{Q}_{\mathrm{rad},3}$ [W]	ø	ø	18.737	ø	ø	9.43
$\dot{Q}_{\mathrm{lead},0}$ [W]	0.074	0.052	0.004	0.094	0.082	0.083
$\dot{Q}_{\mathrm{lead},1}$ [W]	30.765	24.258	0.211	30.999	23.05	22.977
$\dot{Q}_{\mathrm{lead},2}$ [W]	ø	21.738	31.988	ø	20.784	15.596
$\dot{Q}_{\mathrm{lead},3}$ [W]	ø	ø	28.952	ø	ø	13.857
$\dot{Q}_{\mathrm{struc},0}$ [W]	0.155	0.147	0.036	0.157	0.153	0.153
$\dot{Q}_{\mathrm{struc},1}$ [W]	1.187	0.725	0.144	1.181	0.714	0.71
$\dot{Q}_{\mathrm{struc},2}$ [W]	ø	0.471	0.697	ø	0.471	0.271
$\dot{Q}_{\mathrm{struc},3}$ [W]	ø	ø	0.467	ø	ø	0.203
$\dot{Q}_{\mathrm{C},0}$ [W]	0.484	0.435	0.077	0.517	0.492	0.493
$\dot{Q}_{\mathrm{C},1}$ [W]	45.57	30.385	0.777	45.759	29.089	28.962
$\dot{Q}_{\mathrm{C},2}$ [W]	ø	28.771	41.045	ø	27.882	16.086
$\dot{Q}_{\mathrm{C},3}$ [W]	ø	ø	38.457	ø	ø	16.605
$\dot{W}_0$ [W]	901.1	843.5	198.4	556.9	530.2	530.6
$\dot{W}_1$ [W]	1335.6	969	161.5	1284.9	834.9	830.8
$\dot{W}_2$ [W]	ø	44.8	1060.5	ø	43.4	25.3
$\dot{W}_3$ [W]	ø	ø	59.2	ø	ø	9
Cryo. cap [k$]	55	62.5	77.5	30	37.5	45
Cond. cap [k$]	24.6	23.3	17.4	139.4	139.4	139.4
Elec. NPV [k$]	32	26.6	21.2	26.4	20.2	20
Total Cost [k$]	111.7	112.4	116.1	195.7	197	204.3
Total Cost [$/hr]	0.780	0.785	0.811	1.366	1.375	1.426

3.3. Nb-Ti benchmark

We have intentionally focused on conductors that scale to high fields, however the investigation would be incomplete without mention of Nb-Ti. In this section, we briefly present the optimal cost and magnet temperature of Nb-Ti to benchmark the results above. A Nb-Ti conductor is considered that was recently procured at Lawrence Berkeley National Laboratory. The conductor area is scaled to obtain a comparable operating current with the results above, yielding an area of 3.135mm^2, a conductor cost of \$2.85/m and a current of 1575 A at 5 T and 4.2 K. The Bottura relation [26] is then used to find the temperature and field dependent critical current with an 80% operating margin.

The total cost of Nb-Ti as a function of T_C is shown in Fig. 10 with a single thermal intercept and MLI ($\dot{Q}^{\mathrm{MLI}}_{\mathrm{rad,i}}$, Eq. 9). The minimum total cost of \$116.1k is found at T_C = 6.8 K and T_M = 72.3 K with an operating current of 338.7 A. Remarkably, the optimized Nb-Ti design costs \$4.4k more than the optimized Nb_3Sn design at 9.4 K. The optimization was repeated with artificially decreased Nb-Ti conductor costs, and it was found that Nb_3Sn remains the cheaper alternative for Nb-Ti conductor cost reductions up to 20%. To explore an alternative regime, the conductor area was scaled to obtain a reduced operating current of 100 A and the optimization converged on 6.2 K; this magnet temperature is higher than typical conduction cooled LTS systems.

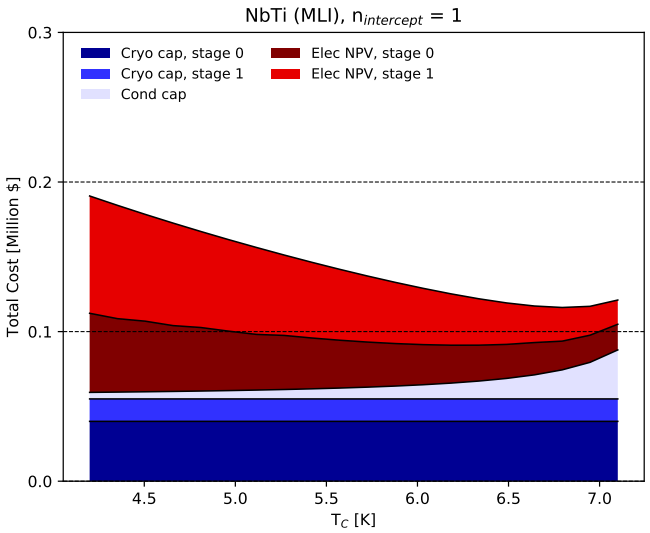

Figure 10: Optimal composition of cost as a function of T_C for Nb-Ti with a single thermal intercept for the low heat load scenario ($\dot{Q}^{\mathrm{MLI}}_{\mathrm{rad,i}}$, Eq. 9).

3.4. Sensitivity Analysis

Based on the analysis above, Nb_3Sn and Bi-2223 with a single thermal interface and MLI ($\dot{Q}^{\mathrm{MLI}}_{\mathrm{rad,i}}$) have been identified as promising configurations. Table 5 presents a sensitivity analysis of these designs, showing the percent change in total cost with a 1 % perturbation of the listed parameter. The sensitivity analysis is ordered by the relative impact on Bi-2223. The most sensitive parameters of Nb_3Sn are the environmental temperature, which drive the warm stage radiation and cryocooler capital cost. The most sensitive parameters of Bi-2223 pertain to increased conductor procurement.

A notable result in Table 5 is the impact of the conductor field strength on Nb_3Sn; increasing the magnetic field on the conductor decreases the total system cost (without considering the additional current that would be required to generate the increased field). This highlights the importance of low operating currents in conduction cooled magnets, where the reduced cryocooler electrical costs from a lower magnet current outweigh the increased conductor capital cost associated with a reduced critical current. In practice, a quench protection analysis would provide a lower bound on the operating current. Another notable result is the high sensitivity of total cost to electricity price, suggesting that Nb_3Sn will be penalized in European countries with higher electricity prices.

Table 5: Sensitivity Analysis of optimized Nb_3Sn and Bi-2223 designs with a single thermal intercept and MLI ($\dot{Q}^{\mathrm{MLI}}_{\mathrm{rad,i}}$, Eq. 9). Columns show percent change in total cost ($\Delta Z_{\mathrm{gantry}}$) with 1% increase in listed parameter.

Δ Parameter [1%]	Nb_3Sn $\Delta Z_{\mathrm{gantry}}$ [%]	Bi-2223 $\Delta Z_{\mathrm{gantry}}$ [%]
Total current (I_{tot})	0.22	0.72
Critical current (I_{c})	-0.11	-0.65
Winding perimeter (P_{magnet})	0.22	0.72
Conductor price (c_{cond})	0.22	0.72
Room temperature (T_{H})	0.66	0.34
HT Cryo. Cost	0.13	0.15
LT Cryo. Cost	0.36	0.00
Cryo. efficiency ($\eta_{II,\mathrm{cryo}}$)	-0.29	-0.14
Electricity price c_{elec}	0.29	0.13
Field on conductor	-0.12	0.12
Lead heat leak ($\dot{Q}_{\mathrm{lead}}$)	0.13	0.07
Num. MLI layers ($\mathrm{n_{MLI}}$)	-0.12	-0.05
Magnet radius	0.11	0.05
Magnet mass	0.04	0.02

4. Discussion

Although Nb_3Sn results in a lower superconducting system cost than Bi-2223, there are a number of advantages for each conductor that are difficult to capture in a model. Nb_3Sn requires a high temperature heat treatment that complicates the manufacturing process. In contrast, the Bi-2223 (and REBCO) tapes are ready to wind as received from the manufacturer. Along the same argumentation, the Nb_3Sn magnet would likely need to be trained with a series of quenches, which is a costly and time-consuming process introducing uncertainty into an assembly line. A Bi-2223 magnet can be tested in liquid nitrogen, potentially reducing magnet QA costs. The Bi-2223 case has the additional advantage of thermal stability over Nb_3Sn at elevated temperatures, where the thermomagnetic properties facilitate recovery from thermal disturbances. Compared to Nb_3Sn, however, Bi-2223 has increased magnetization effects that require experimental demonstration of the achievable field quality for this application. In summary, both conductors show economic promise and have high field properties relevant for a carbon version of the fixed-field gantry, however the results here corroborate the recommendation in Ref. [6] to explore Bi-2223 in superconducting gantries.

It is often mentioned that costs are reduced with high temperature superconductors operating at elevated temperatures, however there has been a lack of quantitative support. Although the results for this application suggest cost savings with magnet temperatures above 4.2 K, benefits are shown to diminish quickly beyond 10 K. This validates the importance of quantifying capital and operating costs in magnet analysis. In addition, the total cost sensitivity to interface temperatures (Fig. 3 and Fig. 4) demonstrates the need for realistic cryogenics designs in thermoeconomic models. Given the value and relative simplicity of the approach, we encourage future conductor and operating temperature evaluations to consider optimization within a thermoeconomic framework across a range of potential magnet applications.

In this work, the beam optics and magnet design are decoupled from the cost analysis by considering the amount of conductor required to generate the prescribed amount of Amp-turns. There is an opportunity to simultaneously couple beam optics and thermoeconomic costing in a magnet optimization, allowing a comparison of magnet designs across a range of magnetic field strengths. This will be explored in future works for both proton and carbon therapy.

5. Conclusion

Motivated by a recent fixed-field gantry concept [5] and a subsequent investigation of Bi-2223 for proton therapy [6], a thermoeconomic model has been developed for a multi-stage, conduction cooled gantry layout. The cryocooler operating cost, cryocooler capital cost and conductor capital cost were analyzed for Nb-Ti, Nb_3Sn, REBCO and Bi-2223, and the optimal thermal intercept temperatures were found with a differential evolution

algorithm. Although Nb_3Sn yielded the lowest cost of \$111.7k over a 20 year lifetime with a single optimized intercept, Bi-2223 was in the realm of feasibility with a lifetime cost of \$195.7k. With the addition investment of \$84k, the Bi-2223 solution offers reduced manufacturing costs (no heat treatment or quench training) and improved thermal stability (higher operating temperature, thermal margin, specific heat and cryocooler cooling power). Remarkably, the optimized Nb-Ti configuration cost more than the Nb_3Sn design. Future work will focus on integrating the thermoeconomic cost model into the coupled magnet design and beam optics optimization, and extend the methodology to thermonuclear fusion reactors [27].

Acknowledgments

This work was supported by the Director, Office of Science, High Energy Physics, and U.S. Department of Energy under contract No. DE-AC02-05CH11231.

References

[1] Jonathan B. Farr, Jacob B. Flanz, Alexander Gerbershagen, and Michael F. Moyers. New horizons in particle therapy systems. *Medical Physics*, 45(11):e953–e983, November 2018.

[2] Alexander Gerbershagen, Ciro Calzolaio, David Meer, Stéphane Sanfilippo, and Marco Schippers. The advantages and challenges of superconducting magnets in particle therapy. *Superconductor Science and Technology*, 29(8):083001, August 2016.

[3] Yoshiyuki Iwata, Mamiko Nishiuchi, Estuo Noda, Koji Noda, Hironao Sakaki, Naoya Saotome, Yuichi Saraya, Shinji Sato, Toshiyuki Shirai, Ryohei Tansho, Takashi Fujita, Tetsuya Fujimoto, Takuji Furukawa, Yousuke Hara, Kiminori Kondo, Kota Mizushima, Takeshi Murakami, and Masayuki Muramatsu. Development of Carbon-Ion Radiotherapy Facilities at NIRS. *IEEE Transactions on Applied Superconductivity*, 28(3):4400807, 2018.

[4] Steven van de Water, Sairos Safai, Jacobus M. Schippers, Damien C. Weber, and Antony J. Lomax. Towards FLASH proton therapy: the impact of treatment planning and machine characteristics on achievable dose rates. *Acta Oncologica*, 58(10):1463–1469, October 2019.

[5] Lucas Brouwer, Anthony Huggins, and Weishi Wan. An achromatic gantry for proton therapy with fixed-field superconducting magnets. *International Journal of Modern Physics A*, 34(36):1942023, December 2019.

[6] Arno Godeke, Luis Alberty, Ender Akcöltekin, Romain Babouche, Clément Detourbe, Rob Nast, Christoph Radermacher, Heinrich Röcken, André Roth, Michael Schillo, Peter vom Stein, Matthew Walpole, Jürgen Wittschen, Kazuhiko Hayashi, Eiji Shizuya, Erik Krooshoop, Ruben Lubkemann, Arend Nijhuis, Cris Vermeer, Alexander Wessel, Jens Krause, Jan Wiezoreck, Alexander Otto, and Linda Saraco. Research at Varian on Applied Superconductivity for Proton Therapy. *Superconductor Science and Technology*, March 2020.

[7] M.A. Green and B.P. Strauss. The Cost of Superconducting Magnets as a Function of Stored Energy and Design Magnetic Induction Times the Field Volume. *IEEE Transactions on Applied Superconductivity*, 18(2):248–251, June 2008.

[8] M. A. Green and B. P. Strauss. Estimating the Operating Cost of Superconducting Magnet Systems at Various Operating Temperatures. *IEEE Transactions on Applied Superconductivity*, 26(4):1–5, June 2016.

[9] M P Oomen, B ten Haken, M Leghissa, and J Rieger. Optimum working temperature of power devices

based on Bi-2223 superconductors. *Superconductor Science and Technology*, 13(10):L19–L24, October 2000.

[10] Sangkwon Jeong and Youngkwon Kim. Thermal anchoring of conduction-cooled current leads for superconductivity applications near liquid nitrogen temperature. *Cryogenics*, 50(4):287–291, April 2010.

[11] Ho-Myung Chang, Yeon Suk Choi, and Steven W. Van Sciver. Optimization of operating temperature in cryocooled HTS magnets for compactness and efficiency. *Cryogenics*, 42(12):787–794, December 2002.

[12] R. Bjørk, K. K. Nielsen, C. R. H. Bahl, A. Smith, and A. C. Wulff. Comparing superconducting and permanent magnets for magnetic refrigeration. *AIP Advances*, 6(5):056205, May 2016.

[13] Reed Teyber and Andrew Rowe. Superconducting magnet design for magnetic liquefiers using total cost minimization. *Cryogenics*, 99:114–122, April 2019.

[14] H.J.M. ter Brake and G.F.M. Wiegerinck. Low-power cryocooler survey. *Cryogenics*, 42(11):705–718, November 2002.

[15] M A Green, S S Chouhan, C Wang, and A F Zeller. Second stage cooling from a Cryomech PT415 cooler at second stage temperatures up to 300 K with cooling on the first-stage from 0 to 250 W. *IOP Conference Series: Materials Science and Engineering*, 101:012002, December 2015.

[16] David Pérez Caparrós. CryoModel: a cryostat thermal performance simulation tool. Technical Report CERN-ATS-Note-2011-087 TECH, CERN, October 2011.

[17] C. W. Keller, G. R. Cunnington, and A. P. Glassford. Final Report - Thermal Performance of Multilayer Insulations. Technical Report NAS 3-14377, Lockheed Missiles & Space Co, 1974.

[18] X. L. Wang, W. Maschmann, J. Eschke, O. Sawlanski, R. Klos, K. Jensch, and B. Petersen. Thermal performance analysis and measurements for the accelerator prototype modules of European XFEL. 2011. Proc. Tesla Technology Collaboration Meeting, Beijing 2011.

[19] Mitsuho Furuse, Koh Agatsuma, and Shuichiro Fuchino. Evaluation of loss of current leads for HTS power apparatuses. *Cryogenics*, 49(6):263–266, June 2009.

[20] A Godeke, B ten Haken, H H J ten Kate, and D C Larbalestier. A general scaling relation for the critical current density in Nb $_3$ Sn. *Superconductor Science and Technology*, 19(10):R100–R116, October 2006.

[21] Y Ilyin, A Nijhuis, and E Krooshoop. Scaling law for the strain dependence of the critical current in an advanced ITER Nb $_3$ Sn strand. *Superconductor Science and Technology*, 20(3):186–191, March 2007.

[22] Yifei Zhang, Traute F. Lehner, Toru Fukushima, Hisaki Sakamoto, and Drew W. Hazelton. Progress in Production and Performance of Second Generation (2G) HTS Wire for Practical Applications. *IEEE Transactions on Applied Superconductivity*, 24(5):7500405, October 2014.

[23] L D Cooley, A K Ghosh, and R M Scanlan. Costs of high-field superconducting strands for particle accelerator magnets. *Superconductor Science and Technology*, 18(4):R51–R65, April 2005.

[24] A Vostner, M Jewell, I Pong, N Sullivan, A Devred, D Bessette, G Bevillard, N Mitchell, G Romano, and C Zhou. Statistical analysis of the Nb_3Sn strand production for the ITER toroidal field coils. *Superconductor Science and Technology*, 30(4):045004, April 2017.

[25] Rainer Storn and Kenneth Price. Differential Evolution - A Simple and Efficient Heuristic for Global Optimization over Continuous Spaces. *Journal of Global Optimization*, 11:341–359, 1997.

[26] L. Bottura. A practical fit for the critical surface of NbTi. *IEEE Transactions on Appiled Superconductivity*, 10(1):1054–1057, March 2000.

[27] D. G. Whyte, J. Minervini, B. LaBombard, E. Marmar, L. Bromberg, and M. Greenwald. Smaller & Sooner: Exploiting High Magnetic Fields from New Superconductors for a More Attractive Fusion Energy Development Path. *Journal of Fusion Energy*, 35(1):41–53, February 2016.